


Waveform systematics in gravitational-wave inference of signals from binary neutron star merger models incorporating higher-order modes information

A. B. Yelikar^{1,*}, R. O’Shaughnessy¹, J. Lange^{2,1} and A. Z. Jan^{2,1}

¹*Center for Computational Relativity and Gravitation, Rochester Institute of Technology, Rochester, New York 14623, USA*

²*Center for Gravitational Physics, University of Texas at Austin, Austin, Texas 78712, USA*

 (Received 26 April 2024; accepted 28 June 2024; published 10 September 2024)

Accurate information from gravitational wave signals from coalescing binary neutron stars (BNSs) provides essential input to downstream interpretations, including inference of the neutron star population and equation of state. However, even adopting the currently most accurate and physically motivated models available for parameter estimation of BNSs, these models remain subject to waveform modeling uncertainty: differences between these models may introduce biases in recovered source properties. In this work, we describe injection studies investigating these systematic differences between the two best waveform models available for BNSs currently, NRHybSur3dq8Tidal and TEOBResumS. We demonstrate that, for BNS sources observable by current second-generation detectors, differences for low-amplitude signals are significant for certain sources.

DOI: [10.1103/PhysRevD.110.064024](https://doi.org/10.1103/PhysRevD.110.064024)

I. INTRODUCTION

Since the discovery of gravitational waves from GW150914 [1], the Advanced Laser Interferometer Gravitational-Wave Observatory (LIGO) [2] and Virgo [3,4] detectors continue to discover gravitational waves (GWs) from coalescing binary black holes (BBHs) and binary neutron stars (BNSs). The properties of each source are inferred by comparing each observation to some estimate(s), commonly called an approximant, for the GWs emitted when a binary merges. As illustrated recently with GW190521 [5,6], GW190814 [7], and GW190412 [8], and the discussion for GWTC-3 [9–11], these approximations have enough differences with respect to each other to produce noticeable differences in inferred posterior distributions, consistent with prior work [12–14]. Despite ongoing generation of new waveforms with increased accuracy [15–20], these previous investigations suggest that waveform model systematics can remain a limiting factor in inferences about individual events [12] and populations [14,21–23], even with contemporary observations.

Future ground- and space-based GW instruments will identify sources with even larger amplitude, further exaggerating the impact of systematic differences between waveform models [14,24]. Investigations using contemporary approximations [10], extensions of post-Newtonian approximations [25], and even numerical relativity simulations [26,27] highlight the extreme challenges faced by

waveform developers preparing for future gravitational wave detectors.

Waveform systematics could be particularly pernicious for detailed analyses to infer the nuclear equation of state from GW observations. For analyses not involving post-merger physics, these approaches look for the subtle impact of matter on the premerger inspiral radiation, due to tidal deformations and altered inspiral rate [28–34]. Even though the GW signal from the early inspiral is well understood because tidal effects are small and accumulate only at the very end of the inspiral, they are embedded deep within the most challenging strong field component of the GW signal. One known limitation of most previous investigations of waveform systematics for BNSs is the neglect of higher-order modes (HOMs). Current state-of-the-art BNS models TEOBResumS [35] and NRHybSur3dq8Tidal [36] incorporate higher-order modes enabling the exploration of these effects. For example, GW190412 [8], which was a merger of two black holes that were highly asymmetric in masses, $30M_{\odot}$ and $8M_{\odot}$, demonstrated the existence and importance of HOMs in parameter inference of GWs from binary mergers [11]. Using models that incorporate HOMs can significantly impact the inferred parameters of sources identified with current-generation instruments for GW170817 or GW170817-like signals, as demonstrated in [37,38]. Despite their expected significance to parameter inference, most studies of BNS systematics omit them and rarely perform large-scale parameter inference studies to fully assess the impact of systematics, although a similar study was done in [39]. For example, several

*Contact author: ay2016@rit.edu

mismatch studies are mostly done for models having only leading-order (2,2) mode [40–42]. A study done with fiducial BNS signals with HOMs argued that biases in inferring the reduced tidal parameter could be larger than the statistical 90% only for very high SNR signals ~ 80 [28] in the LIGO-Virgo band. Recent work by Narikawa [43] looked at the effects of multipoles by comparing the MultipoleTidal model to PNTidal and NRTidalv2 waveforms, showing that mismatches and phases do differ between them for systems with higher mass and large tidal deformabilities.

In this work, we demonstrate systematic differences between parameter inferences of synthetic BNS sources performed with different waveform models. Unlike previous studies, which focused on different mass scales (e.g., BBH) or different amplitude scales (e.g., SNR greater than 80, more pertinent to third-generation instruments [25]), our study emphasizes the interpretation of near-threshold detections. Even though some events have nearly identical interpretations independent of the waveform model, we show that frequently low-amplitude BNS observations have somewhat different inferred properties, depending on the waveform model used to interpret them. These differences contradict conventional rules of thumb based on waveform mismatches, which suggest that, for low-amplitude signals whose waveforms are sufficiently similar, no differences in parameter inference are expected. However, for the low amplitudes involved in our study, we also find these differences are not driven by the higher-order mode content of the waveform, in contrast to systematic differences seen when analyzing louder BNS signals with HOMs [37,38].

This paper is organized as follows. In Sec. II, we review the use of the Rapid Iterative FiTting (RIFT) algorithm for parameter inference; the waveform models used in this work; and the techniques used in [44] to assess systematic error. We describe one fiducial ensemble of synthetic sources, targeted at the most common (low) amplitude sources. In Sec. III, we use two well-studied waveform models to demonstrate the impact of contemporary model systematics. We show that model systematics will be important, at a level which must impact population results and consistency tests like PP plots. In Sec. IV, we summarize our results and discuss their potential applications to future GW sources and population inference.

II. METHODS

A. RIFT review

A coalescing compact binary in a quasicircular orbit can be completely characterized by its intrinsic and extrinsic parameters. By intrinsic parameters, we refer to the binary's detector-frame masses m_i , spins χ_i , and any quantities characterizing matter in the system, Λ_i . The masses are expressed in terms of quantities chirp-mass (\mathcal{M}) and mass ratio (q) that better characterize the leading-order dependence of the gravitational wave phase than do the individual

masses. By extrinsic parameters, we refer to the seven numbers needed to characterize its spacetime location and orientation: luminosity distance (d_L), right ascension (α), declination (δ), inclination (ι), polarization (ψ), coalescence phase (ϕ_c), and time (t_c). We will express masses in solar mass units and dimensionless nonprecessing spins in terms of Cartesian components aligned with the orbital angular momentum $\chi_{i,z}$, as we use waveform models that do not account for precession. We will use λ , θ to refer to intrinsic and extrinsic parameters, respectively.

$$\lambda: (\mathcal{M}, q, \chi_{1,z}, \chi_{2,z}, \Lambda_1, \Lambda_2)$$

$$\theta: (d_L, \alpha, \delta, \iota, \psi, \phi_c, t_c)$$

RIFT [45,46] consists of a two-stage iterative process to interpret gravitational wave data d via comparison to predicted gravitational wave signals $h(\lambda, \theta)$. In one stage, for each λ_β from some proposed “grid” $\beta = 1, 2, \dots, N$ of candidate parameters, RIFT computes a marginal likelihood

$$\mathcal{L}_{\text{marg}} \equiv \int \mathcal{L}(\lambda, \theta) p(\theta) d\theta \quad (1)$$

from the likelihood $\mathcal{L}(\lambda, \theta)$ of the gravitational wave signal in the multidetector network, accounting for detector response; see the RIFT paper for a more detailed specification [45,46]. In the second stage, RIFT performs two tasks. First, it generates an approximation to $\mathcal{L}(\lambda)$ based on its accumulated archived knowledge of marginal likelihood evaluations ($\lambda_\beta, \mathcal{L}_\beta$). This approximation can be generated by Gaussian processes, random forests, or other suitable approximation techniques. Second, using this approximation, it generates the (detector-frame) posterior distribution:

$$p_{\text{post}} = \frac{\mathcal{L}_{\text{marg}}(\lambda) p(\lambda)}{\int d\lambda \mathcal{L}_{\text{marg}}(\lambda) p(\lambda)}, \quad (2)$$

where prior $p(\lambda)$ is the prior on intrinsic parameters like mass and spin. The posterior distribution is produced by performing a Monte Carlo integral: the evaluation points and weights in that integral are weighted posterior samples, which are fairly resampled to generate conventional independent, identically distributed “posterior samples.” For further details on RIFT's technical underpinnings and performance, see [45–48].

B. Waveform models

The tidal waveform models used in this study are IMRPhenomD_NRTidalv2, NRHybSur3dq8Tidal, and TEOB-ResumS. NRTidalv2 models [49] are improved versions of NRTidal [50] models, which are closed-form tidal approximants for binary neutron star coalescence and have been analytically added to selected binary black hole GW models to obtain a binary neutron star waveform,

TABLE I. List of runs for low-amplitude signals.

Injection model	Recovery model
NRHybSur3dq8Tidal($\ell = 5$)	NRHybSur3dq8Tidal($\ell = 5$)
NRHybSur3dq8Tidal($\ell = 5$)	NRHybSur3dq8Tidal($\ell = 2$)
NRHybSur3dq8Tidal($\ell = 5$)	TEOBResumS($\ell = 4$)
NRHybSur3dq8Tidal($\ell = 5$)	IMRPhenomD_NRTidalv2
NRHybSur3dq8Tidal($\ell = 5$)	IMRPhenomD
TEOBResumS($\ell = 4$)	TEOBResumS($\ell = 4$)
TEOBResumS($\ell = 4$)	NRHybSur3dq8Tidal($\ell = 5$)
TEOBResumS($\ell = 4$)	IMRPhenomD_NRTidalv2
TEOBResumS($\ell = 4$)	IMRPhenomD

either in the time domain or in the frequency domain. The NRHybSur3dq8Tidal [36] tidal model is based on the binary black hole hybrid model NRHybSur3dq8, which is constructed via an interpolation of NR waveforms. It includes all modes $\ell \leq 4$, $(5, \pm 5)$ but not $(4, \pm 1)$ and $(4, 0)$ and models tidal effects up to $\Lambda_{1,2} < 5000$. This model combines the accuracy of surrogate waveforms with the efficiency of PN models. TEOBResumS [35] is another but unique time-domain EOB formalism that includes tidal effects for all modes $\ell \leq 4$ but not $m = 0$ and models tidal effects up to $\Lambda_{1,2} < 5000$ and for spins up to 0.5.

C. Fiducial synthetic sources and PP tests

We consider one universe of 100 synthetic signals for a 3-detector network (HLV), with masses drawn uniformly in m_i in the region bounded by $\mathcal{M}/M_\odot \in [1.2, 1.4]$, $\eta \in [0.2, 0.25]$, and Λ for each object uniformly distributed up to 1000. The tidal deformability values are not drawn according to any $M - \Lambda$ relation. These bounds are expressed in terms of $\mathcal{M} = (m_1 m_2)^{3/5} / (m_1 + m_2)^{1/5}$ and $\eta = m_1 m_2 / (m_1 + m_2)^2$ and encompass the detector-frame parameters of neutron stars observed to date [51–53]. The extrinsic parameters are drawn uniformly in the sky position and isotropically in Euler angles, with source luminosity distances drawn proportional to d_L^2 between 90 and 240 Mpc for low SNR injections. All our sources have nonprecessing spins, with each component assumed to be uniform between $[-0.05, 0.05]$; this is due to limitations of the NRHybSur3dq8Tidal model.

For complete reproducibility, we use NRHybSur3dq8Tidal, TEOBResumS, and IMRPhenomD_NRTidalv2, starting the signal evolution and likelihood integration at 30 Hz, performing all analysis with 4096 Hz time series in Gaussian noise with known advanced LIGO design PSDs [54]. The BNS signal is generated for 300 seconds, but analysis was performed only on 128 seconds of data. For each synthetic event and interferometer, we use the same noise realization for all waveform approximations. Therefore, the differences between them arise solely due to waveform systematics. The NRHybSur3dq8Tidal

model is utilized with two settings: (a) $\ell = 5$ and (b) $\ell = 2$, which includes only the dominant quadrupole mode. TEOBResumS and IMRPhenomD_NRTidalv2 approximants are used with $\ell = 4$ and $\ell = 2$ settings, respectively. Table I lists the various settings of the waveform models used in parameter inference in this work.

Figure 1 shows the cumulative SNR distribution (under a “zero-noise” assumption) of the specific synthetic population generated from this distribution. Compared to GW170817’s confident detection, which was a BNS merger that occurred at 40 Mpc detected by LIGO-Virgo with a SNR of 32.4, the majority of the signals in this fiducial population have SNRs below or near the typical detection criteria for a BNS merger, with some having high enough amplitudes.

By using a very modest-amplitude population to assess the impact of waveform systematics, we demonstrate their immediate impact on the kinds of analyses currently being performed on real observations, let alone future studies.

One way to assess the performance of parameter inference is a probability–probability plot (usually denoted PP plot) [55]. Using RIFT on each source k , with true parameters λ_k , we estimate the fraction of the posterior distributions which is below the true source value $\lambda_{k,\beta}$ [$\hat{P}_{k,\beta}(< \lambda_{k,\beta})$] for each intrinsic parameter β . After reindexing the sources so $\hat{P}_{k,\beta}(\lambda_{k,\beta})$ increases with k for some fixed β , the panels of Fig. 5, for example, show a plot of k/N versus $\hat{P}_k(\lambda_{k,\beta})$ for all binary parameters for different scenarios.

D. JS test

To more sharply identify subtle differences introduced by waveform systematics, we will directly compare pairs of inferred posterior probability distributions deduced with different waveforms but from the same set of data to each other. Many pairwise error diagnostics have been used in the literature in general and with RIFT in particular [46]. In this study, motivated by previous work [56], we use the one-dimensional Jensen-Shannon (JS) divergence $J(p, q) = (D(q|m) + D(p|m))$, where

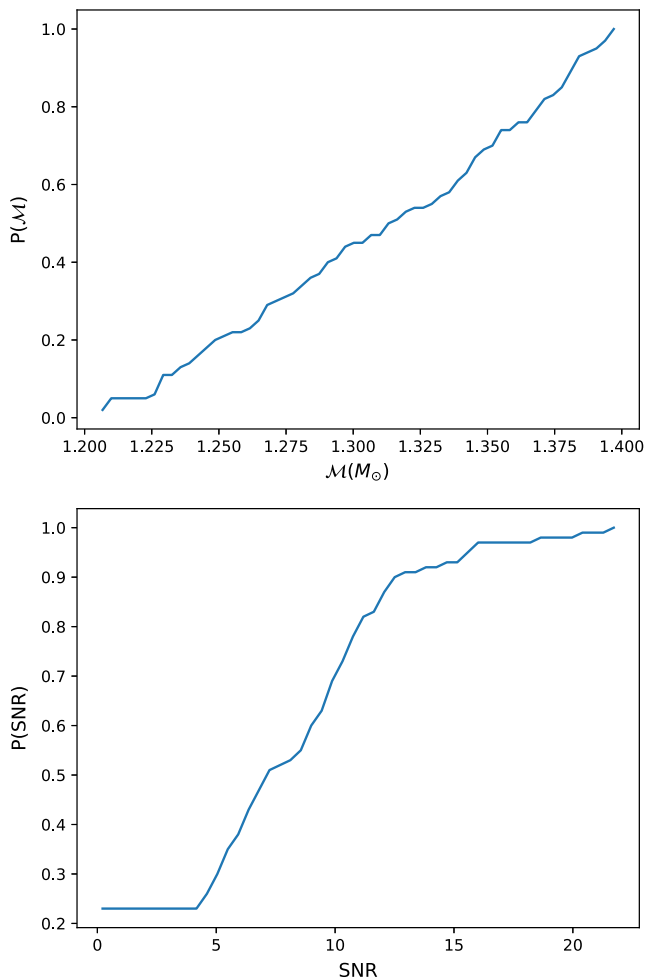


FIG. 1. Top panel: cumulative distribution of the chirp-mass for a synthetic population of 100 events each drawn from the fiducial BNS population described in Sec. II C. Bottom panel: cumulative SNR distribution for the same population. To avoid ambiguity, this figure shows the expected SNR (i.e., the SNR evaluated using a zero-noise realization).

$D(a|b) = \int dx a(x) \log_2 a(x)/b(x)$ and $m = (a + b)/2$. The JS divergence is symmetric and ranges between 0 (for identical distributions) and 1. For the multidimensional problems described here, we adopt the median JS divergence over all parameters. Analyses of O3 using multiple waveforms suggest that binary black holes analyzed with different contemporary waveforms will produce answers differing by $O(0.02)$ [57–59].

III. RESULTS

Our investigations corroborate our central expectation: inferences computed with different waveforms are frequently substantially different, even for BNS and even for near-threshold events. The most extreme contrast appeared between TEOBResumS and other waveform models, where for our near-threshold synthetic events we found ubiquitous qualitatively different inferences.

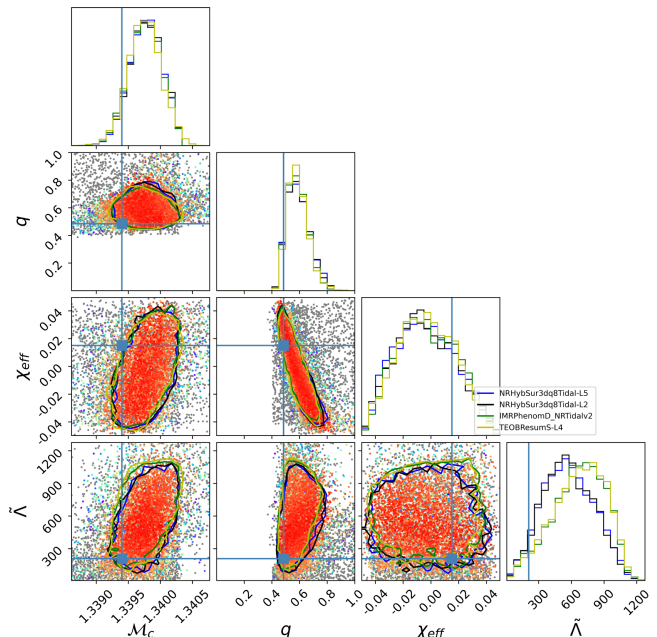


FIG. 2. Corner plot showing recovered 1D distributions of \mathcal{M} , q , χ_{eff} , and $\tilde{\Lambda}$ for a low-amplitude NRHybSur3dq8Tidal-lmax5 injection (crosshairs indicate true value) analyzed with various waveform models listed in the legend. The JS divergence value associated with this event is 0.027.

A. Anecdotal examples

As an illustrative example of the systematics explored more comprehensively in the population studies below, Fig. 2 shows the results of parameter inference using multiple recovery waveforms applied to the same synthetic data source, here a low-amplitude NRHybSur3dq8Tidal-lmax5 injection. Despite its low signal amplitude, this example shows that posterior distributions derived from the same synthetic data will differ, depending on the GW signal model used to interpret it.

B. JS divergences: Demonstrating and quantifying waveform systematics

Figure 3 shows the cumulative distribution of combined JS divergences of parameters \mathcal{M} , q , χ_{eff} , and $\tilde{\Lambda}$, between analyses performed with NRHybSur3dq8Tidal $\ell_{\text{max}} = 5$ low amplitude injections. Specifically, the JS divergence is calculated between an analysis performed using precisely the same model used for injections on the one hand, and the alternative model listed in the legend on the other. Inferences performed with all state-of-the-art models that include tidal physics often produce qualitatively similar inferences, with JS divergences typically less than 10^{-2} . Some relatively modest disagreement is expected between (a) different waveform models and (b) the expected modest impact of higher-order modes for low-mass sources. By contrast, more than 10% of inferences have JS divergences larger than 10^{-1} (mean over all parameters) in all cases

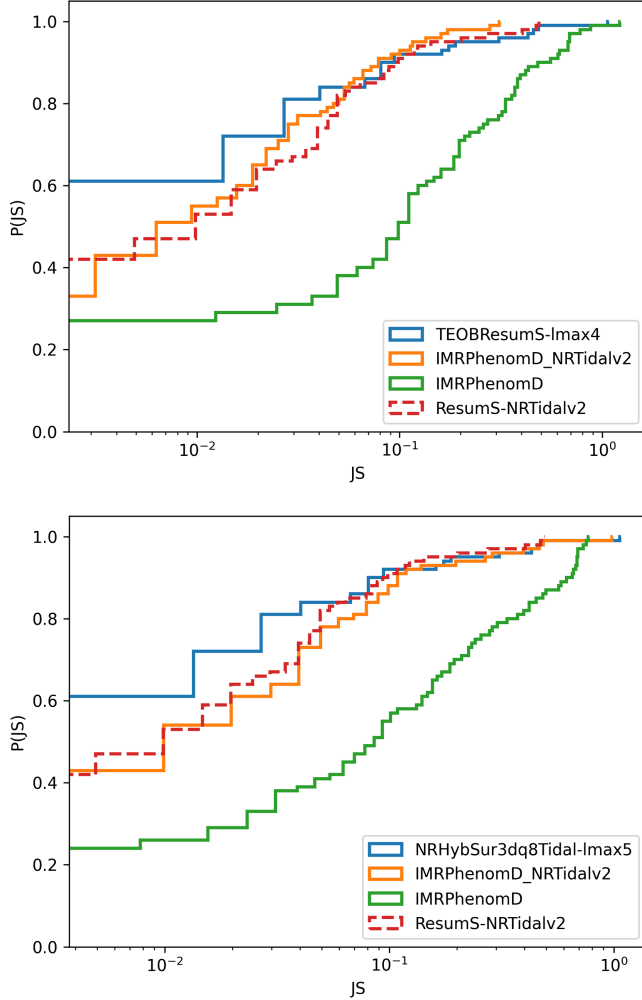


FIG. 3. JS divergence values of parameters \mathcal{M} , q , χ_{eff} , and $\tilde{\Lambda}$ distribution for analysis on different recovery waveform models with low-amplitude NRHybSur3dq8Tidal-Imax5 injections. Top panel: each JS divergence used in the CDF is performed between the parameter estimation (PE) constructed with the indicated model and reference PE constructed with NRHybSur3dq8. Bottom panel: same as above, but using TEOBReumS for the reference PE.

when using models that include similar mode content (but a different waveform model). These calculations suggest that *frequently, both* waveform systematics *and* higher-order modes produce noticeably different results.

The green line in Fig. 3 shows that tides must be included to avoid significantly biasing the interpretation of a typical low-amplitude source. This JS divergence corresponds to inferences that neglect tides entirely (via a point-particle IMRPhenomD model), even though the true full model includes tides. In this case, the JS divergence is frequently larger than 0.1, indicating substantial disagreement with the best possible interpretation.

To investigate the impact of waveform systematics specifically, we computed mismatches between the injected and inference waveform (2,2) modes. We employ only

the (2,2) mode in our mismatch comparisons due to the limitations of one of our waveform models, which contains only this mode and its conjugate (2, -2) mode. That said, for nonprecessing binary neutron stars, most of the strain power and information content is contained within the dominant quadrupole mode. *Mismatch* is a simple inner-product-based estimate of waveform similarity between two model predictions [14,60–65] $h_1(\lambda)$ and $h_2(\lambda)$ at identical model parameters λ :

$$\mathcal{M}(\lambda) = 1 - \max_{t_c, \phi_c} \frac{|\langle h_1 | e^{i(2\pi f t_c + \phi_c)} h_2 \rangle|}{|h_1| |h_2|}. \quad (3)$$

In this expression, the inner product $\langle a | b \rangle_k \equiv \int_{-\infty}^{\infty} 2df \tilde{a}(f)^* \tilde{b}(f) / S_{h,k}(|f|)$ is implied by the k th detector’s noise power spectrum $S_{h,k}(f)$, which for the purposes of waveform similarity is assumed to be the advanced LIGO instrument, H1. In practice, we adopt a low-frequency cutoff f_{min} so all inner products are modified to

$$\langle a | b \rangle_k \equiv 2 \int_{|f| > f_{\text{min}}} df \frac{[\tilde{a}(f)]^* \tilde{b}(f)}{S_{h,k}(|f|)}. \quad (4)$$

The left panel of Fig. 4 shows the results for NRHybSur3dq8Tidal injections recovered with TEOBResumS, with the mismatch shown as a color scale on top of the injected source SNR and cumulative JS divergence (summed over four one-dimensional JS divergences for parameters \mathcal{M} , q , χ_{eff} , and $\tilde{\Lambda}$). While the mismatches are within the waveform accuracy requirements [66] for most of the injections ($> 10^{-2}$), higher mismatches don’t correlate well with extreme JS divergences. Rather, below some modest SNR, the random noise realization seems to interact adversely with these large mismatches to produce nearly unconstrained posterior distributions, such that the similarity between inferences *becomes stochastic and diverges* at low amplitude. The right panel of Figure 4 shows qualitatively similar behavior, using comparisons of NRHybSur3dq8Tidal and IMRPhenomD_NRTidalv2.

C. PP plots

The differences between waveforms are significant enough that their imprint can even impact bulk diagnostics such as a PP plots [44], which average the impact of waveform systematics over a large population of randomly chosen events.

Figures 5 and 6 provide another representation of the analyses presented above in the context of JS divergence: synthetic sources generated with the NRHybSur3dq8Tidal ($\ell_{\text{max}} = 5$) and TEOBResumS ($\ell_{\text{max}} = 4$) models. In each panel, colored dots show the empirical cumulative distribution of the posterior quantiles of the injections—the PP plot for each parameter, with colors corresponding to the

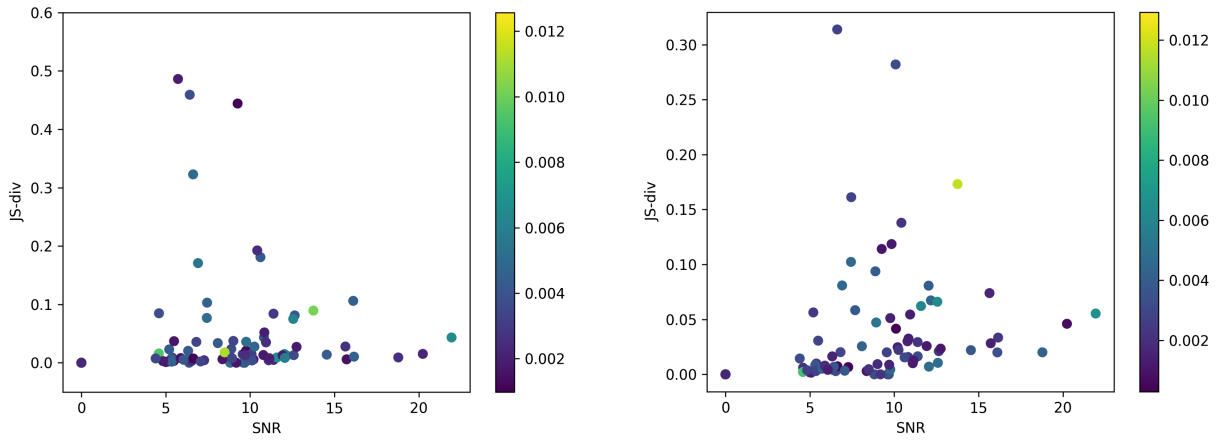


FIG. 4. Left panel: zero-noise SNR v/s JS divergence (cumulative of \mathcal{M} , q , χ_{eff} , and $\tilde{\Lambda}$) between NRHybSur3dq8Tidal ($\ell_{\text{max}} = 5$) and TEOBResumS ($\ell_{\text{max}} = 4$) for the NRHybSur3dq8Tidal low-amplitude injections. Color scale shows the mismatch between NRHybSur3dq8Tidal and TEOBResumS. Right panel: same as left panel, except for NRHybSur3dq8Tidal and IMRPhenomD_NRTidalv2. Note the mismatches are calculated for the dominant (2,2) mode only.

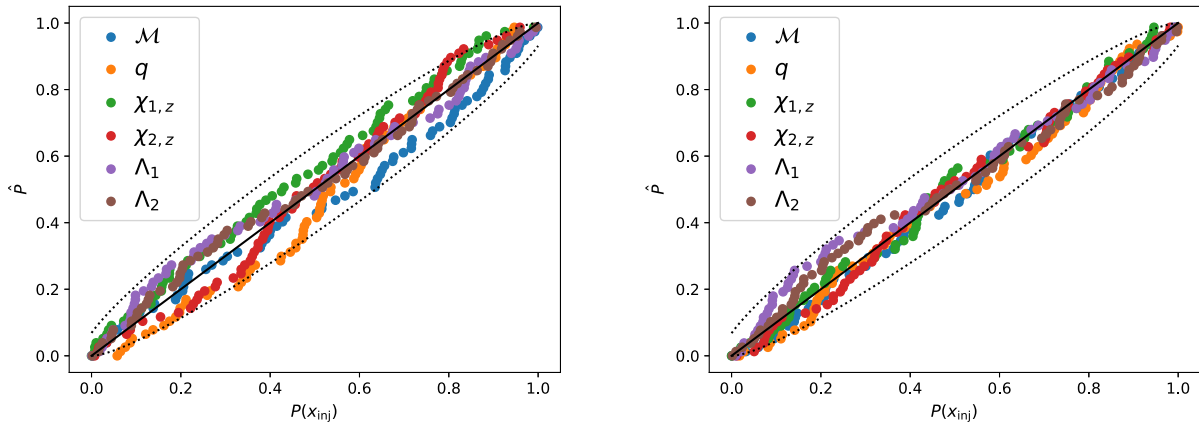


FIG. 5. PP plot of low-amplitude injections with NRHybSur3dq8Tidal with all higher-order modes ($\ell_{\text{max}} = 5$) on the left and TEOBResumS with all higher-order modes ($\ell_{\text{max}} = 4$) on the right recovered with the same model as the injection. Both sets have the same injection parameters. The dashed line indicates the 90% credible interval expected for a cumulative distribution drawn from 100 uniformly distributed samples.

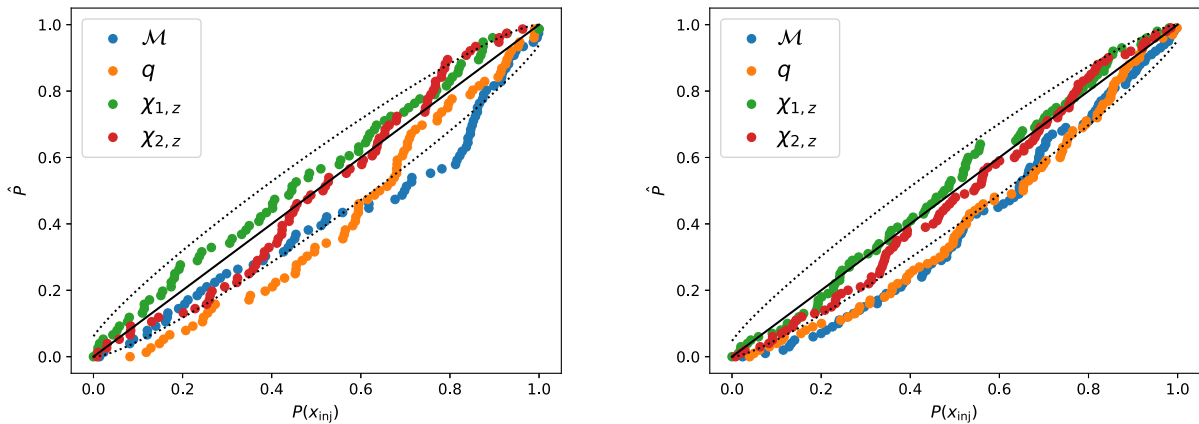


FIG. 6. PP plot of low-amplitude injections with NRHybSur3dq8Tidal with all higher-order modes ($\ell_{\text{max}} = 5$) on the left and TEOBResumS with all higher-order modes ($\ell_{\text{max}} = 4$) on the right recovered with IMRPhenomD. Both sets have the same injection parameters. The dashed line indicates the 90% credible interval expected for a cumulative distribution drawn from 100 uniformly distributed samples.

parameters indicated in the legend. Figure 5, in which the same model was used for both injection and recovery for a particular panel, shows that PP plots for every parameter are consistent with $P(< p) = p$, as expected. However, Fig. 6 where analyses used IMRPhenomD for recovery, shows that omitting tidal physics entirely can bring in distinct inconsistencies with $P = p$ for injections where tides are significant and important.

IV. CONCLUSIONS

In this paper, we demonstrated that the interpretation of typical low-amplitude BNS sources will frequently exhibit noteworthy differences, depending on the adopted model for analysis. Specifically, we showed that a JS divergence between inferences constructed between two different state-of-the-art waveforms would be larger than 10^{-1} for a significant population of mergers. These large differences persist even though the mismatch between the dominant $(2, \pm 2)$ modes of this state-of-the-art waveforms is small, and even though the SNR of our test sources is low. Additionally, corroborating previous work [43,67], we demonstrate that tidal effects are essential to include even in interpreting our population of modest SNR sources. Specifically, we showed that neglecting tidal physics in parameter inference causes a PP plot to deviate significantly from the expected diagonal behavior, indicating a biased recovery of mass and/or spin parameters.

Our study stands in contrast with the expectations of several previous studies, which have argued that the effects of waveform systematics for these low-mass, low-amplitude sources will be small. For example, investigations done in [28] suggest that systematic differences will supersede statistical differences for sources only for high SNR for the current GW detectors.

Our investigation only demonstrated notable differences in the conclusions derived from different waveform models. Further study is required to assess to what extent

these differences propagate into conclusions derived from a population of sources or if they average out over the population.

ACKNOWLEDGMENTS

The authors would like to thank Carl-Johan Haster for helpful comments. R. O. S. gratefully acknowledges support from NSF Grant No. NSF PHY-1912632, No. PHY-2012057, No. AST-1909534, and No. PHY-2309172 and Simons Foundation. A. Y. acknowledges support from Grant No. NSF PHY-2012057. This material is based upon work supported by NSF's LIGO Laboratory which is a major facility fully funded by the National Science Foundation. This research has made use of data, software, and/or web tools obtained from the Gravitational Wave Open Science Center [68], a service of LIGO Laboratory, the LIGO Scientific Collaboration and the Virgo Collaboration. LIGO Laboratory and Advanced LIGO are funded by the United States National Science Foundation (NSF) as well as the Science and Technology Facilities Council (STFC) of the United Kingdom, the Max-Planck-Society (MPS), and the State of Niedersachsen/Germany for support of the construction of Advanced LIGO and construction and operation of the GEO600 detector. Additional support for Advanced LIGO was provided by the Australian Research Council. Virgo is funded through the European Gravitational Observatory (EGO), by the French Centre National de Recherche Scientifique (CNRS), the Italian Istituto Nazionale di Fisica Nucleare (INFN), and the Dutch Nikhef, with contributions by institutions from Belgium, Germany, Greece, Hungary, Ireland, Japan, Monaco, Poland, Portugal, and Spain. The authors are grateful for computational resources provided by the LIGO Laboratory and supported by National Science Foundation Grant No. PHY-0757058, No. PHY-0823459, and No. PHY-1626190, and IUCAA LDG cluster Sarathi.

-
- [1] B. Abbott *et al.* (The LIGO Scientific and the Virgo Collaborations), *Phys. Rev. Lett.* **116**, 061102 (2016).
 - [2] J. Aasi, B. P. Abbott, R. Abbott, T. Abbott, M. R. Abernathy, K. Ackley, C. Adams, T. Adams, P. Addesso *et al.* (LIGO Scientific Collaboration), *Classical Quantum Gravity* **32**, 074001 (2015).
 - [3] T. Accadia *et al.*, *J. Instrum.* **7**, P03012 (2012).
 - [4] F. Acernese *et al.* (Virgo Collaboration), *Classical Quantum Gravity* **32**, 024001 (2015).
 - [5] B. P. Abbott, R. Abbott, T. D. Abbott, S. Abraham, F. Acernese, K. Ackley, C. Adams, V. B. Adya *et al.* (The LIGO Scientific and the Virgo Collaborations), *Phys. Rev. Lett.* **125**, 101102 (2020).
 - [6] B. P. Abbott, R. Abbott, T. D. Abbott, S. Abraham, F. Acernese, K. Ackley, C. Adams, V. B. Adya *et al.* (The LIGO Scientific and the Virgo Collaborations), *Astrophys. J. Lett.* **900**, L13 (2020).
 - [7] B. P. Abbott, R. Abbott, T. D. Abbott, S. Abraham, F. Acernese, K. Ackley, C. Adams, V. B. Adya *et al.* (The LIGO Scientific and the Virgo Collaborations), *Astrophys. J. Lett.* **896**, L44 (2020).
 - [8] B. P. Abbott, R. Abbott, T. D. Abbott, S. Abraham, F. Acernese, K. Ackley, C. Adams, V. B. Adya *et al.* (The

- LIGO Scientific and the Virgo Collaborations), *Phys. Rev. D* **102**, 043015 (2020).
- [9] R. Abbott *et al.* (LIGO Scientific, Virgo, and KAGRA Collaborations), *Phys. Rev. X* **13**, 041039 (2023).
- [10] Q. Hu and J. Veitch, *Phys. Rev. D* **106**, 044042 (2022).
- [11] T. Islam, S. E. Field, C.-J. Haster, and R. Smith, *Phys. Rev. D* **103**, 104027 (2021).
- [12] F. H. Shaik, J. Lange, S. E. Field, R. O'Shaughnessy, V. Varma, L. E. Kidder, H. P. Pfeiffer, and D. Wysocki, *Phys. Rev. D* **101**, 124054 (2020).
- [13] A. Williamson, J. Lange, R. O'Shaughnessy, J. Clark, P. Kumar, J. Bustillo, and J. Veitch, *Phys. Rev. D* **96**, 124041 (2017).
- [14] M. Pürrer and C.-J. Haster, *Phys. Rev. Res.* **2**, 023151 (2020).
- [15] M. Hannam, P. Schmidt, A. Bohé, L. Haegel, S. Husa, F. Ohme, G. Pratten, and M. Pürrer, *Phys. Rev. Lett.* **113**, 151101 (2014).
- [16] S. Khan, K. Chatziioannou, M. Hannam, and F. Ohme, *Phys. Rev. D* **100**, 024059 (2019).
- [17] A. Bohé, L. Shao, A. Taracchini, A. Buonanno, S. Babak, I. W. Harry, I. Hinder, S. Ossokine, M. Pürrer, V. Raymond *et al.*, *Phys. Rev. D* **95**, 044028 (2017).
- [18] V. Varma, S. E. Field, M. A. Scheel, J. Blackman, D. Gerosa, L. C. Stein, L. E. Kidder, and H. P. Pfeiffer, *Phys. Rev. Res.* **1**, 033015 (2019).
- [19] G. Pratten, C. García-Quirós, M. Colleoni, A. Ramos-Buades, H. Estellés, M. Mateu-Lucena, R. Jaume, M. Haney, D. Keitel, J. E. Thompson *et al.*, *Phys. Rev. D* **103**, 104056 (2021).
- [20] S. Ossokine, A. Buonanno, S. Marsat, R. Cotesta, S. Babak, T. Dietrich, R. Haas, I. Hinder, H. P. Pfeiffer, M. Pürrer *et al.*, *Phys. Rev. D* **102**, 044055 (2020).
- [21] D. Wysocki, J. Lange, and R. O'Shaughnessy, *Phys. Rev. D* **100**, 043012 (2019).
- [22] V. Kapil, L. Reali, R. Cotesta, and E. Berti, *Phys. Rev. D* **109**, 104043 (2024).
- [23] A. Dhani, S. Völkel, A. Buonanno, H. Estelles, J. Gair, H. P. Pfeiffer, L. Pompili, and A. Toubiana, [arXiv:2404.05811](https://arxiv.org/abs/2404.05811).
- [24] N. Afshordi, S. Akçay, P. Amaro Seoane, A. Antonelli, J. C. Aurekoetxea, L. Barack, E. Barausse, R. Benkel, L. Bernard *et al.* (LISA Consortium Waveform Working Group), [arXiv:2311.01300](https://arxiv.org/abs/2311.01300).
- [25] C. B. Owen, C.-J. Haster, S. Perkins, N. J. Cornish, and N. Yunes, *Phys. Rev. D* **108**, 044018 (2023).
- [26] D. Ferguson, K. Jani, P. Laguna, and D. Shoemaker, *Phys. Rev. D* **104**, 044037 (2021).
- [27] A. Jan, D. Ferguson, J. Lange, D. Shoemaker, and A. Zimmerman, [arXiv:2312.10241](https://arxiv.org/abs/2312.10241).
- [28] R. Gamba, M. Breschi, S. Bernuzzi, M. Agathos, and A. Nagar, *Phys. Rev. D* **103**, 124015 (2021).
- [29] T. Narikawa and N. Uchikata, *Phys. Rev. D* **106**, 103006 (2022).
- [30] K. Chatziioannou, *Phys. Rev. D* **105**, 084021 (2022).
- [31] N. Kunert, P. T. H. Pang, I. Tews, M. W. Coughlin, and T. Dietrich, *Phys. Rev. D* **105**, L061301 (2022).
- [32] G. Ashton and T. Dietrich, *Nat. Astron.* **6**, 961 (2022).
- [33] G. Riemenschneider, P. Rettegno, M. Breschi, A. Albertini, R. Gamba, S. Bernuzzi, and A. Nagar, *Phys. Rev. D* **104**, 104045 (2021).
- [34] M. Favata, *Phys. Rev. Lett.* **112**, 101101 (2014).
- [35] A. Nagar, S. Bernuzzi, W. Del Pozzo, G. Riemenschneider, S. Akçay, G. Carullo, P. Fleig, S. Babak, K. W. Tsang, M. Colleoni *et al.*, *Phys. Rev. D* **98**, 104052 (2018).
- [36] K. Barkett, Y. Chen, M. A. Scheel, and V. Varma, *Phys. Rev. D* **102**, 024031 (2020).
- [37] J. Lange, R. O'Shaughnessy, K. Barkett, V. Varma, and S. Field, in *APS April Meeting Abstracts* (American Physical Society, New York, 2022), Vol. 2022, p. D17.007.
- [38] J. Calderón Bustillo, S. H. W. Leong, T. Dietrich, and P. D. Lasky, *Astrophys. J. Lett.* **912**, L10 (2021).
- [39] Y. Huang, C.-J. Haster, S. Vitale, V. Varma, F. Foucart, and S. Biscoveanu, *Phys. Rev. D* **103**, 083001 (2021).
- [40] A. Samajdar and T. Dietrich, *Phys. Rev. D* **98**, 124030 (2018).
- [41] A. Samajdar and T. Dietrich, *Phys. Rev. D* **100**, 024046 (2019).
- [42] T. Dietrich, T. Hinderer, and A. Samajdar, *Gen. Relativ. Gravit.* **53**, 27 (2021).
- [43] T. Narikawa, *Phys. Rev. D* **108**, 063029 (2023).
- [44] A. Z. Jan, A. B. Yelikar, J. Lange, and R. O'Shaughnessy, *Phys. Rev. D* **102**, 124069 (2020).
- [45] J. Lange, R. O'Shaughnessy, and M. Rizzo, [arXiv:1805.10457](https://arxiv.org/abs/1805.10457).
- [46] J. Wofford, A. B. Yelikar, H. Gallagher, E. Champion, D. Wysocki, V. Delfavero, J. Lange, C. Rose, V. Valsan, S. Morisaki *et al.*, *Phys. Rev. D* **107**, 024040 (2023).
- [47] D. Wysocki, R. O'Shaughnessy, J. Lange, and Y.-L. L. Fang, *Phys. Rev. D* **99**, 084026 (2019).
- [48] J. Lange, RIFT'ing the Wave: Developing and applying an algorithm to infer properties gravitational wave sources (2020), <https://dcc.ligo.org/LIGO-P2000268>.
- [49] T. Dietrich, A. Samajdar, S. Khan, N. K. Johnson-McDaniel, R. Dudi, and W. Tichy, *Phys. Rev. D* **100**, 044003 (2019).
- [50] T. Dietrich, S. Bernuzzi, and W. Tichy, *Phys. Rev. D* **96**, 121501 (2017).
- [51] B. P. Abbott, R. Abbott, T. D. Abbott, F. Acernese, K. Ackley, C. Adams, T. Adams, P. Addesso *et al.* (The LIGO Scientific and the Virgo Collaborations), *Phys. Rev. Lett.* **119**, 161101 (2017).
- [52] B. P. Abbott, R. Abbott, T. D. Abbott *et al.*, *Astrophys. J. Lett.* **892**, L3 (2020).
- [53] R. Abbott *et al.* (LIGO Scientific, KAGRA, and Virgo Collaborations), *Astrophys. J. Lett.* **915**, L5 (2021).
- [54] LIGO Scientific Collaboration (2018), <https://dcc.ligo.org/LIGO-T1800044>.
- [55] S. Cook, A. Gelman, and D. Rubin, *J. Comput. Graph. Stat.* **15**, 675 (2006).
- [56] G. Ashton and C. Talbot, *Mon. Not. R. Astron. Soc.* **507**, 2037 (2021).
- [57] B. P. Abbott, R. Abbott, T. D. Abbott, F. Acernese, K. Ackley, C. Adams, T. Adams, P. Addesso *et al.* (The LIGO Scientific and The Virgo Collaborations), *Phys. Rev. X* **9**, 031040 (2019).
- [58] R. Abbott, T. D. Abbott, S. Abraham, F. Acernese, K. Ackley, A. Adams, C. Adams, R. X. Adhikari *et al.* (LIGO Scientific and Virgo Collaborations), *Phys. Rev. X* **11**, 021053 (2021).

- [59] T. Islam, A. Vajpeyi, F. H. Shaik, C.-J. Haster, V. Varma, S. E. Field, J. Lange, R. O’Shaughnessy, and R. Smith, [arXiv:2309.14473](https://arxiv.org/abs/2309.14473).
- [60] L. Lindblom, B. J. Owen, and D. A. Brown, *Phys. Rev. D* **78**, 124020 (2008).
- [61] J. S. Read, C. Markakis, M. Shibata, K. Uryū, J. D. E. Creighton, and J. L. Friedman, *Phys. Rev. D* **79**, 124033 (2009).
- [62] L. Lindblom, J. G. Baker, and B. J. Owen, *Phys. Rev. D* **82**, 084020 (2010).
- [63] H. Cho, E. Ochsner, R. O’Shaughnessy, C. Kim, and C. Lee, *Phys. Rev. D* **87**, 024004 (2013).
- [64] M. Hannam, S. Husa, F. Ohme, and P. Ajith, *Phys. Rev. D* **82**, 124052 (2010).
- [65] P. Kumar, T. Chu, H. Fong, H. P. Pfeiffer, M. Boyle, D. A. Hemberger, L. E. Kidder, M. A. Scheel, and B. Szilagyi, *Phys. Rev. D* **93**, 104050 (2016).
- [66] S. Khan, S. Husa, M. Hannam, F. Ohme, M. Pürrer, X. J. Forteza, and A. Bohé, *Phys. Rev. D* **93**, 044007 (2016).
- [67] R. Dudi, F. Pannarale, T. Dietrich, M. Hannam, S. Bernuzzi, F. Ohme, and B. Brügmann, *Phys. Rev. D* **98**, 084061 (2018).
- [68] <https://www.gw-openscience.org/>.